Discrete cavity dynamics in free-space Brillouin laser

Jiabao Peng,[1,2,*] Longjie Zhang,[3,4,5,*] Zhenxu Bai,[3,4,5,†] Stephan Fritzsche,[1,2,‡] and Zhiwei Lu[3,4,5,§]
[1]*Helmholtz-Institut Jena, Fröbelstieg 3, 07743 Jena, Germany*
[2]*Theoretisch-Physikalisches Institut, Friedrich-Schiller-Universitat Jena, D-07743 Jena, Germany*
[3]*Center for Advanced Laser Technology, Hebei University of Technology, Tianjin 300401, China*
[4]*Hebei Key Laboratory of Advanced Laser Technology and Equipment, Tianjin 300401, China*
[5]*Collaborative Innovation Center for Diamond Laser Technology and Applications, Tianjin 300401, China*

(Received 26 April 2026; accepted 9 July 2026; published 27 July 2026)

Highly coherent lasers are central to modern photonics. To date, high-coherence operation has been achieved predominantly in microcavity and fiber-based platforms. More recently, free-space Brillouin-laser experiments have revealed unusually strong noise suppression whose physical origin cannot be explained by conventional continuous-medium models developed for those platforms. In conventional continuous-medium models, the optical and acoustic fields are assumed to remain continuously coupled throughout the cavity evolution, whereas in free-space implementations the coupling is confined to the nonlinear medium and interrupted by passive propagation over the rest of the round trip. To describe this interaction-propagation separation, we develop a discrete-cavity model in which the short Brillouin interaction inside the gain medium and the subsequent free-space propagation are treated as two separate stages of the round-trip evolution. This separation introduces a temporal asymmetry between optical storage and acoustic relaxation, effectively enhancing acoustic damping at the cavity level and strongly reducing pump-noise transfer to the Stokes field. When the cavity round-trip time is much longer than the nonlinear interaction time in the gain medium, the predicted noise-suppression ratio is governed by the ratio between these two timescales. These results identify the discrete interaction-propagation structure as the physical origin of the unusually strong noise suppression in free-space Brillouin laser systems.

DOI: 10.1103/vhpb-kl3z

I. INTRODUCTION

Highly coherent lasers are essential for a wide range of precision measurement applications, including optical atomic clocks [1,2], quantum information processing [3,4], gravitational-wave detection [5,6], and high-resolution spectroscopy [7]. Conventional routes to narrow-linewidth and low-noise laser operation include frequency stabilization with high-Q cavities [8], distributed-feedback architectures [9], nonplanar ring oscillators [10], and stimulated Brillouin scattering (SBS) in fiber and integrated photonic platforms [11,12]. Among these approaches, Brillouin lasers have emerged as a particularly important platform for narrow-linewidth optical generation, low-noise microwave synthesis, and integrated coherent photonics [13–19]. Their coherence enhancement arises from the large separation between the acoustic damping rate and the optical decay rate. Fast pump-phase fluctuations cannot efficiently drive the acoustic mode and are therefore only weakly transferred to the Stokes field, leading to substantial linewidth narrowing and reduced noise. Early Brillouin lasers were realized mainly in optical fibers [20–25], where long interaction lengths enable efficient SBS at low threshold. More recently, microcavity and on-chip Brillouin lasers have demonstrated exceptionally narrow linewidths, low thresholds, and operation across different spectral regions within spatially continuous cavity-media configurations [26–28]. These continuously coupled systems are well described by established Brillouin-laser noise and linewidth theories [29,30].

Whereas continuous-medium Brillouin lasers have achieved narrow linewidths and strong noise suppression in guided and monolithic platforms, a recent free-space Brillouin-laser experiment [31] reported remarkably low noise levels and strong noise suppression, pointing to the potential of this platform for high-power, ultralow-noise operation. In particular, the observed noise-suppression ratios substantially exceed the predictions of conventional continuous-medium theories that have successfully described fiber and microresonator Brillouin lasers [29,30]. In these conventional models, the optical and acoustic fields are treated as copropagating and continuously coupled within the same nonlinear gain medium throughout the cavity evolution. This framework successfully accounts for linewidth narrowing, noise suppression, and noise transfer in guided Brillouin-laser platforms. In a free-space Brillouin laser, however, the optical and acoustic fields do not remain continuously coupled throughout the cavity round trip [32,33]. The optical field interacts with the acoustic field only during the short passage through the gain medium, whereas a substantial fraction of each round trip consists of passive free-space propagation.

*These authors contributed equally to this work.
†Contact author: baizhenxu@hotmail.com
‡Contact author: s.fritzsche@gsi.de
§Contact author: zhiweilv@hebut.edu.cn

During this passive stage, the optical field continues to circulate in the cavity, while the acoustic field remains confined to the gain medium and relaxes independently. Conventional continuous-medium models therefore fail to reproduce the experimentally observed degree of noise suppression in free-space systems, suggesting that key physical mechanisms are not captured in existing theoretical descriptions.

To describe free-space Brillouin lasers theoretically, we develop a discrete-cavity model. In Sec. II, we first review the conventional continuous-medium description of the three-wave coupled equations for Brillouin interactions, in which the evolution of the optical and acoustic fields is governed by coupled differential equations. In Sec. III, we introduce the discrete-cavity formulation, where the continuous time derivatives in the conventional model are replaced by a round-trip iterative map. This discrete-cavity formulation naturally incorporates the free-space propagation between successive interactions in the gain medium. In Sec. IV, we solve the discrete iterative model by determining its fixed points and derive the corresponding threshold condition. In Sec. V, we then analyze the noise properties of the system by applying a discrete Fourier transform to the linearized dynamics to derive the noise-transfer relations and evaluate both the relative intensity noise and the fundamental linewidth. Finally, Sec. VI summarizes the main results and discusses their implications.

II. CONTINUOUS-MEDIUM MODEL FOR BRILLOUIN LASERS

We begin from the electromagnetic wave equation in a dielectric medium,

$$\nabla^2\mathbf{E} - \frac{n^2}{c^2}\frac{\partial^2\mathbf{E}}{\partial t^2} = \frac{1}{\epsilon_0 c^2}\frac{\partial^2\mathbf{P}}{\partial t^2}, \tag{1}$$

where $\mathbf{E}$ is the electric field, n is the refractive index of the medium, c is the speed of light in vacuum, and ϵ_0 is the vacuum permittivity. The nonlinear polarization $\mathbf{P}$ is induced by electrostriction. For the SBS process, the optical field is decomposed into forward-propagating pump and backward-propagating Stokes components with slowly varying envelopes:

$$\begin{aligned}E_p(\mathbf{r},t) &= \tfrac{1}{2}\psi_p(x,y)A_p(z,t)e^{i(k_p z-\omega_p t)} + \text{c.c.},\\ E_s(\mathbf{r},t) &= \tfrac{1}{2}\psi_s(x,y)A_s(z,t)e^{i(-k_s z-\omega_s t)} + \text{c.c.}\end{aligned} \tag{2}$$

The electrostrictive modulation of the refractive index gives rise to the nonlinear polarization

$$P(\mathbf{r},t) = \epsilon_0\rho_m^{-1}\gamma_e\,\psi_\rho(x,y)\tilde{\rho}(z,t)\,E(\mathbf{r},t), \tag{3}$$

where γ_e is the electrostrictive constant. The total mass-density distribution is written as

$$\tilde{\rho}(z,t) = \rho_m + \tfrac{1}{2}\rho(z,t)e^{i(qz-\Omega t)} + \text{c.c.}, \tag{4}$$

where ρ_m denotes the equilibrium mass density of the medium and $\rho(z,t)$ is the slowly varying complex amplitude of the acoustic density wave.

Substituting Eqs. (2) and (3) into Eq. (1), and applying the slowly varying envelope approximation, we retain only the resonant terms satisfying the SBS energy and momentum conservation conditions, $\omega_p = \omega_s + \Omega$ and $k_p = k_s + q$. Here Ω and q denote the angular frequency and wave vector of the acoustic wave, respectively. Physically, the interference between the pump and Stokes fields produces a beat note that drives a coherent acoustic wave through electrostriction. The resulting density modulation changes the refractive index of the medium and scatters pump photons into the Stokes mode. The SBS process therefore forms a closed three-wave interaction mediated by the acoustic wave. The resulting coupled-mode equations are

$$\begin{aligned}\frac{\partial A_p}{\partial t} &= -\frac{\gamma_p}{2}A_p + \frac{i\omega_p\gamma_e}{4n^2\rho_m}\,\Lambda_p\,\rho\,A_s + \sqrt{\kappa_{\text{ex}}}S_{\text{in}},\\ \frac{\partial A_s}{\partial t} &= -\frac{\gamma_s}{2}A_s + \frac{i\omega_s\gamma_e}{4n^2\rho_m}\,\Lambda_s\,\rho^*A_p,\\ \frac{\partial\rho}{\partial t} &= -\frac{\Gamma_B}{2}\,\rho + \frac{i\epsilon_0\gamma_e^2q^2}{4\Omega}\,\Lambda_\rho\,A_pA_s^*.\end{aligned} \tag{5}$$

In Eqs. (5), γ_p and γ_s denote the decay rates of the pump and Stokes cavity modes, respectively, including intrinsic loss and external coupling. The parameter Γ_B is the acoustic damping rate. The term $\sqrt{\kappa_{\text{ex}}}S_{\text{in}}$ describes injection of the external pump field into the cavity, where S_{in} is the input pump field and κ_{ex} is the external coupling rate. This source term follows the standard input-output formulation of temporal coupled-mode theory, in which the external driving field enters the cavity equation through the factor $\sqrt{\kappa_{\text{ex}}}$ [34]. In the normalization used here, A_p and A_s have units of $\sqrt{\text{energy}}$, so that $|A_p|^2$ and $|A_s|^2$ are proportional to intracavity pump and Stokes energies. The input field S_{in} has units of $\sqrt{\text{power}}$, so that $|S_{\text{in}}|^2$ is proportional to the input pump power. Accordingly, $\sqrt{\kappa_{\text{ex}}}S_{\text{in}}$ has the same units as $\partial_t A_p$ and acts as the driving term for the intracavity pump field.

To include the transverse structure of the optical and acoustic modes, we introduce the overlap factors Λ_p, Λ_s, and Λ_ρ in the three-wave coupling terms. These factors reduce the spatially dependent optoacoustic interaction to an effective single-mode coupling by integrating the transverse field profiles over the interaction area. They quantify the spatial matching between the pump, Stokes, and acoustic modes and therefore renormalize the effective Brillouin coupling strengths. With the mode profiles $\psi_p(x,y)$, $\psi_s(x,y)$, and $\psi_\rho(x,y)$, the overlap factors are defined as

$$\begin{aligned}\Lambda_p &= \frac{\int_A \psi_\rho(x,y)\,\psi_s(x,y)\,\psi_p^*(x,y)\,dA}{\int_A \psi_p(x,y)\,\psi_p^*(x,y)\,dA},\\ \Lambda_s &= \frac{\int_A \psi_\rho^*(x,y)\,\psi_p(x,y)\,\psi_s^*(x,y)\,dA}{\int_A \psi_s(x,y)\,\psi_s^*(x,y)\,dA},\\ \Lambda_\rho &= \frac{\int_A \psi_p(x,y)\,\psi_s^*(x,y)\,\psi_\rho^*(x,y)\,dA}{\int_A \psi_\rho(x,y)\,\psi_\rho^*(x,y)\,dA}.\end{aligned} \tag{6}$$

Here A denotes the transverse interaction area, and the denominators specify the normalization of the corresponding pump, Stokes, and acoustic mode amplitudes.

A representative realization of the continuous-medium picture is the microresonator Brillouin laser illustrated in Fig. 1(a). In this configuration, the pump field circulates in a high-Q microresonator and interacts continuously with

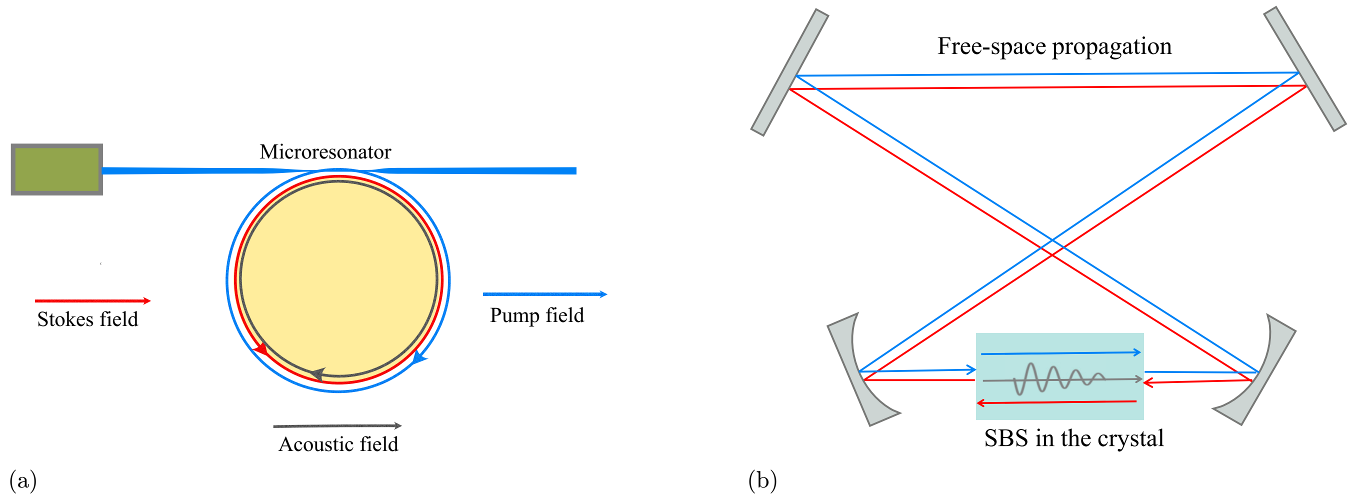

FIG. 1. Comparison of the conventional continuous-medium scheme and the free-space Brillouin laser configuration. (a) Microresonator Brillouin laser with continuous optoacoustic interaction in a colocalized nonlinear medium. (b) Free-space Brillouin laser with localized interaction in the gain crystal and passive propagation over the remainder of the cavity round trip.

the acoustic mode supported by the same structure. The pump field and the acoustic density wave propagate in the same direction to circulate clockwise, while the generated Stokes field propagates in the opposite direction and circulates counterclockwise. This propagation geometry is required by momentum conservation, $k_p = k_s + q$, where the acoustic wave vector q compensates the momentum difference between the forward pump field and the backward Stokes field. Because the pump, Stokes, and acoustic fields remain colocalized within the same nonlinear medium throughout the cavity evolution, this system is well described by the continuous-medium three-wave model. Within this model, the transfer of pump-phase noise to the Stokes field is controlled by the competition between the acoustic relaxation rate and the optical decay rate of the Stokes mode. Physically, strong acoustic damping filters fast pump-phase fluctuations: these fluctuations are mainly taken up by the acoustic degree of freedom and are therefore only weakly transferred to the Stokes field. As a result, the noise-suppression ratio increases with the ratio between the acoustic damping rate and the Stokes-mode decay rate. For a continuously coupled Brillouin laser, the corresponding low-frequency frequency-noise suppression ratio is conventionally written as [26]

$$\mathcal{C}_{\mathrm{CM}} = \left(1 + \frac{\Gamma_B}{\gamma_s}\right)^2. \tag{7}$$

Here $\mathcal{C}_{\mathrm{CM}}$ is defined as the ratio between the input pump frequency-noise power spectral density and the generated Stokes frequency-noise power spectral density in the low-frequency limit. The squared form therefore reflects the fact that the suppression factor acts on the phase or frequency fluctuation amplitude, whereas $\mathcal{C}_{\mathrm{CM}}$ is a noise-power spectral density ratio.

For high-Q microresonators, $\gamma_s \ll \Gamma_B$, so that a large noise-suppression ratio can be achieved. This mechanism is highly effective in microresonator systems, where the large cavity Q leads to a small optical decay rate, although such devices typically operate at relatively low output power. In free-space Brillouin lasers, however, power scaling generally requires a lower cavity Q and hence a larger optical decay rate than in high-Q microresonator systems [31]. If the conventional continuous-medium model is applied only to the nonlinear gain medium, the predicted suppression remains governed by the local rate ratio Γ_B/γ_s and does not become exceptionally large under realistic free-space operating conditions. In particular, substituting the parameters relevant to the gain region alone does not reproduce the strong noise-suppression ratio observed experimentally. This discrepancy shows that the free-space propagation outside the gain medium cannot be treated as dynamically irrelevant. Instead, it must be incorporated explicitly into the cavity description, since it changes the relative timescales over which optical coupling and acoustic relaxation accumulate. This failure motivates a new cavity-level description in which the localized Brillouin interaction and the subsequent free-space propagation are treated as distinct stages of the round-trip evolution.

III. DISCRETE-CAVITY MODEL

To capture the essential cavity structure of free-space Brillouin lasers, we introduce a discrete-cavity model in which each round trip is separated into a localized Brillouin interaction inside the gain medium and a subsequent passive free-space propagation stage. Unlike in continuous-medium descriptions, the Brillouin interaction is not distributed over the entire cavity path but occurs only during the finite passage through the nonlinear medium. As illustrated in Fig. 1(b), the optical field then continues to circulate through the passive free-space segment, whereas the acoustic field remains confined to the gain medium and relaxes in the absence of further optical driving. Successive Brillouin interactions therefore sample a partially relaxed acoustic field rather than a continuously driven one. From the viewpoint of the round-trip optical dynamics, this interaction–propagation separation appears as an enhanced effective acoustic damping and reduces the transfer of pump fluctuations to the Stokes field. Inspired by the

Ikeda map [35], we formulate the discrete-cavity dynamics by representing the system with a state vector $\mathbf{X}^{(n)}$, which collects the slowly varying amplitudes of the pump field, the Stokes field, and the acoustic density wave immediately before the nth interaction event:

$$\mathbf{X}^{(n)} \equiv \begin{pmatrix} A_p^{(n)} \\ A_s^{(n)} \\ \rho^{(n)} \end{pmatrix}. \tag{8}$$

Here n labels successive cavity round trips, while $A_p^{(n)}$, $A_s^{(n)}$, and $\rho^{(n)}$ denote the pump-field, Stokes-field, and acoustic density-wave amplitudes at the chosen reference plane.

Within the discrete-cavity model, the round-trip dynamics naturally decompose into two successive stages: the nonlinear Brillouin interaction inside the gain medium and the subsequent passive propagation through the free-space cavity. These two processes are described by separate evolution operators. The nonlinear interaction inside the gain medium is represented by an operator $\mathcal{U}_{\rm NL}$, defined as the finite-time evolution generated by the three-wave equations (5) over the interaction time in the nonlinear medium. Acting on the state vector, this operator produces an intermediate state

$$\mathbf{X}^{(n,+)} = \mathcal{U}_{\rm NL}\, \mathbf{X}^{(n)}. \tag{9}$$

The passive free-space propagation between successive interaction events is described by a propagation operator $\mathcal{U}_{\rm free}$. During this stage no Brillouin interaction occurs; the optical fields mainly accumulate propagation phase, while the acoustic field undergoes free decay governed by its intrinsic damping rate. The propagation operator therefore acts diagonally on the state vector,

$$\mathbf{X}^{(n+1)} = \mathcal{U}_{\rm free}\, \mathbf{X}^{(n,+)}, \tag{10}$$

with

$$\mathcal{U}_{\rm free} = \begin{pmatrix} e^{i\phi_p} & 0 & 0 \\ 0 & e^{i\phi_s} & 0 \\ 0 & 0 & e^{-\frac{\Gamma_B}{2}\tau_{\rm fs}} \end{pmatrix}. \tag{11}$$

Here $\tau_{\rm fs}$ denotes the free-space propagation time. The full round-trip time is $\tau_{\rm rt} = \tau_{\rm int} + \tau_{\rm fs}$. Since the interaction time is much shorter than the passive propagation time in the free-space configuration considered here, the acoustic relaxation between two successive interaction events is written in the reduced map in terms of $\tau_{\rm rt}$. The factors $e^{i\phi_p}$ and $e^{i\phi_s}$ represent the phase accumulation of the pump and Stokes fields during the free-space propagation interval. Since the two optical fields remain phase locked in the steady operating regime, these propagation phases do not affect the subsequent coupled dynamics and can be treated as dynamically irrelevant. By contrast, the acoustic component acquires the decay factor $e^{-\frac{\Gamma_B}{2}\tau_{\rm fs}}$, which describes the relaxation of the acoustic field during the same interval. Then evolution over one cavity round trip is therefore described by the discrete map

$$\mathbf{X}^{(n+1)} = (\mathcal{U}_{\rm free} \circ \mathcal{U}_{\rm NL})\mathbf{X}^{(n)}, \tag{12}$$

which explicitly separates the localized nonlinear interaction from the subsequent passive propagation in the cavity.

To obtain an explicit and analytically tractable discrete map for the free-space cavity dynamics, we now introduce a delta-kick approximation for the nonlinear evolution inside the gain medium. In this approximation, the nonlinear interaction operator $\mathcal{U}_{\rm NL}$, which in principle represents the finite-time evolution generated by the full three-wave Brillouin equations, is reduced to a short first-order update during the crystal transit time. The word "delta" is used in analogy with a Dirac-delta-like temporal localization, reflecting that the Brillouin interaction is confined to a short time window rather than being distributed over the full cavity round trip. This reduction is justified when $\tau_{\rm int} \ll \tau_{\rm rt}$ and the optical and acoustic amplitudes vary only weakly during a single pass through the gain medium. Under this approximation, the Brillouin interaction is treated as a localized event that acts once during each cavity round trip, over a finite interaction time $\tau_{\rm int}$ determined by the transit of the optical field through the gain medium. The corresponding fields immediately after the interaction are then obtained by integrating the continuous three-wave equations (5) over a single pass through the medium. To leading order in the interaction time $\tau_{\rm int}$, this procedure yields the following reduced update equations:

$$\begin{aligned} A_p^{(n+1)} &= \left(1 - \frac{\gamma}{2}\tau_{\rm int}\right)A_p^{(n)} + ig_p\,\tau_{\rm int}\,\rho^{(n)}A_s^{(n)} + \sqrt{\kappa_{\rm ex}}\,\tau_{\rm int}\,S_{\rm in}, \\ A_s^{(n+1)} &= \left(1 - \frac{\gamma}{2}\tau_{\rm int}\right)A_s^{(n)} + ig_s\,\tau_{\rm int}\,\rho^{*(n)}A_p^{(n)}, \\ \rho^{(n+1)} &= \left(1 - \frac{\Gamma_B}{2}\tau_{\rm rt}\right)\rho^{(n)} + ig_\rho\,\tau_{\rm int}\,A_p^{(n)}A_s^{*(n)}. \end{aligned} \tag{13}$$

The prefactor $1 - \frac{\gamma}{2}\tau_{\rm int}$ represents the optical survival factor over the short interaction interval $\tau_{\rm int}$, obtained to first order from the continuous optical loss term. Here we assume, for simplicity, that the pump and Stokes fields have the same optical decay rate, $\gamma_p = \gamma_s \equiv \gamma$. By contrast, the factor $1 - \frac{\Gamma_B}{2}\tau_{\rm rt}$ represents the acoustic survival factor over one cavity round trip, reflecting the fact that the acoustic field continues to decay throughout the full round-trip time $\tau_{\rm rt}$, including the passive free-space propagation stage. Under these assumptions, the effective optical and acoustic coupling strengths are given by

$$g_p \equiv \frac{\omega_p\gamma_e}{4n^2\rho_m}\Lambda_p, \quad g_s \equiv \frac{\omega_s\gamma_e}{4n^2\rho_m}\Lambda_s, \quad g_\rho \equiv \frac{\epsilon_0\gamma_e^2q^2}{4\Omega}\Lambda_\rho. \tag{14}$$

The factor $\tau_{\rm int}$ appears because these coefficients describe the nonlinear coupling accumulated during a single passage through the gain medium, rather than the instantaneous coupling rates of the continuous-time equations. The explicit derivation of these coefficients and of the reduced discrete map is given in Appendix A. Here we only summarize the two approximations underlying Eqs. (13). First, the continuous three-wave interaction is coarse grained over the finite interaction time $\tau_{\rm int}$, so that the nonlinear coupling is represented as a single kick acting once per cavity round trip. Second, the interaction is assumed to be sufficiently weak that the pump, Stokes, and acoustic amplitudes do not vary appreciably during one pass through the gain medium, which allows the coupling terms to be evaluated using their preinteraction values.

IV. STEADY-STATE SOLUTIONS AND THRESHOLD CONDITION

We now analyze the steady-state operation of the discrete-cavity Brillouin laser described by Eqs. (13). In the discrete-cavity framework, the steady state is defined as a fixed point of the round-trip map, such that the system state reproduces itself after each cavity round trip:

$$A_p^{(n+1)} = A_p^{(n)},\quad A_s^{(n+1)} = A_s^{(n)},\quad \rho^{(n+1)} = \rho^{(n)}. \tag{15}$$

This fixed-point condition refers to the field values evaluated at a chosen reference plane in the cavity. It does not require the fields to remain constant throughout the round trip. Rather, the steady state corresponds to a periodic dynamical state whose sampled values repeat once per cavity cycle, while the fields may still evolve within each cycle.

At steady state, the field amplitudes remain invariant from one round trip to the next. Substituting the fixed-point condition into Eqs. (13), the lasing threshold is obtained by considering the onset of a nonzero Stokes solution, $A_{s,0} \neq 0$, for which the Brillouin gain exactly compensates the effective cavity losses. This yields the intracavity pump threshold intensity,

$$|A_{p,0}|^2_{\text{th}} = \frac{\gamma\,\Gamma_B}{4g_s g_\rho}\,\frac{\tau_{\text{rt}}}{\tau_{\text{int}}}. \tag{16}$$

The corresponding input-pump threshold then follows from the below-threshold pump relation by setting $A_{s,0} = 0$. Equation (16) shows explicitly that the lasing threshold scales in proportion to the ratio $\tau_{\text{rt}}/\tau_{\text{int}}$. This dependence reflects the fact that the nonlinear interaction is confined to only a short segment of each cavity round trip, so that a longer passive propagation interval requires a correspondingly larger intracavity pump field to reach threshold. Above threshold, the intracavity pump field becomes clamped close to its threshold value. Under this condition, the steady-state Stokes intensity is given by

$$|A_{s,0}|^2 = \frac{\Gamma_B}{2g_s g_\rho}\,\frac{\tau_{\text{rt}}}{\tau_{\text{int}}}\left(\frac{\sqrt{\kappa_{\text{ex}}}\,|S_{\text{in}}|}{|A_{p,0}|_{\text{th}}} - \frac{\gamma}{2}\right). \tag{17}$$

Equation (17) shows that the Stokes intensity scales linearly with the effective pump drive above threshold, while remaining proportional to the ratio $\tau_{\text{rt}}/\tau_{\text{int}}$.

To validate the analytical results, we performed time-domain numerical simulations based on the discrete round-trip formulation in Eq. (12). The parameters used in the simulations are summarized in Table I. In each round trip, the nonlinear three-wave equations were integrated through the diamond gain medium using a fourth-order Runge-Kutta (RK4) scheme, followed by a passive free-space propagation step in which the optical fields evolved freely and the acoustic field decayed over the remaining round-trip time. Figure 2 shows the steady-state output Stokes power as a function of the input pump power. The solid blue curve represents the analytical prediction obtained from Eq. (17), while the open circles denote the numerical solutions of the discrete round-trip map described by Eq. (12). A clear lasing threshold is observed at $P_{\text{th}} \approx 12$ W, above which the Stokes power increases monotonically with the excess pump. The excellent agreement between the analytical curve and the numerical data confirms the validity of the steady-state approximation and the pump-clamping assumption employed in the theoretical derivation. For the parameter set used here, an input pump power of 45 W yields an output Stokes power of approximately 17 W, comparable to the experimentally reported value of 14.6 W at the same pump power [31].

TABLE I. Characteristic parameters of the free-space diamond Brillouin laser used in the simulations.

Parameter	Value
Crystal length, L_c (m)	5.0×10^{-3}
Cavity length, L (m)	5.08×10^{-1}
Refractive index, n	2.39
Acoustic damping rate, Γ_B (MHz)	$2\pi \times 5.3$
Electrostrictive constant, γ_e	8.16
Pump wavelength, λ_p (nm)	1064
Mass density, ρ_m (g/cm^3)	3.515
Acoustic velocity, v (km/s)	18
Beam waist, w_0 (µm)	74
External coupling rate, κ_{ex} (s^{-1})	2.3×10^{7}
Optical cavity decay rate, γ (s^{-1})	3.6×10^{7}
Interaction time, τ_{int} (s)	4.0×10^{-11}
Round-trip time, τ_{rt} (s)	1.7×10^{-9}
Acoustic wavevector, q (m^{-1})	2.8×10^{7}
Acoustic angular frequency, Ω (s^{-1})	5.1×10^{11}
Optical mode volume, V_{opt} (m^3)	8.6×10^{-11}

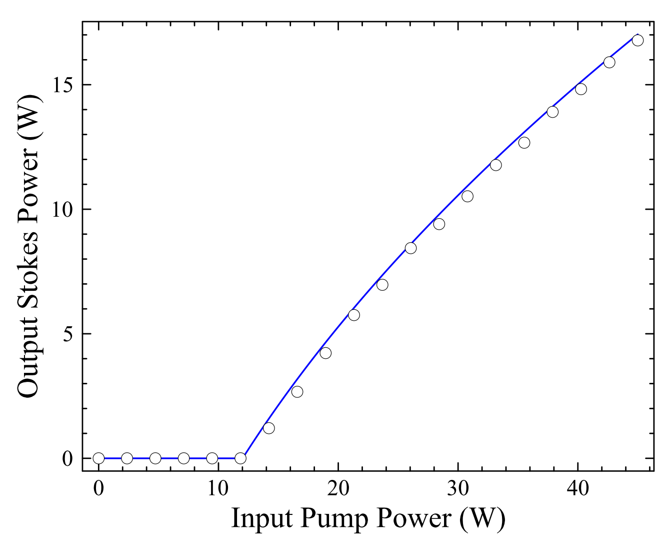

FIG. 2. Steady-state output Stokes power as a function of input pump power. The solid curve represents the analytical steady-state solution of Eq. (17), while circles denote numerical solutions of the discrete-cavity map. The threshold is $P_{\text{th}} \approx 12$ W, above which the Stokes power increases linearly due to pump clamping. At an input pump power of 45 W, the Stokes output power reaches approximately 17 W.

V. NOISE DYNAMICS

A. Noise compression and scaling behavior

To analyze the frequency-domain response of the discrete-cavity Brillouin laser, we now perform a small-signal analysis around the steady-state operating point obtained in Sec. IV. This approach allows us to quantify how weak fluctuations evolve from round trip to round trip and how pump noise is transferred, filtered, or suppressed by the coupled optical-acoustic dynamics. We therefore linearize the round-trip evolution equations, Eqs. (13), about the steady state and introduce small perturbations of the pump, Stokes, and acoustic fields as

$$\begin{aligned} A_p^{(n)} &= A_{p,0} + \delta A_p^{(n)}, \\ A_s^{(n)} &= A_{s,0} + \delta A_s^{(n)}, \\ \rho^{(n)} &= \rho_0 + \delta\rho^{(n)}, \end{aligned} \tag{18}$$

where $\delta A_p^{(n)}$, $\delta A_s^{(n)}$, and $\delta\rho^{(n)}$ represent small perturbations around the steady state. These quantities are generally complex and describe both amplitude and phase fluctuations of the fields. Substituting these expressions into Eqs. (13) and retaining only first-order terms yields the linearized evolution equations:

$$\begin{aligned} \delta A_p^{(n+1)} &= \Big(1 - \frac{\gamma}{2}\tau_{\rm int}\Big)\delta A_p^{(n)} + ig_p\,\tau_{\rm int}\big(\rho_0\,\delta A_s^{(n)} + A_{s,0}\,\delta\rho^{(n)}\big) \\ &\quad + \sqrt{\kappa_{\rm ex}}\,\tau_{\rm int}\,\delta S_{\rm in}^{(n)}, \\ \delta A_s^{(n+1)} &= \Big(1 - \frac{\gamma}{2}\tau_{\rm int}\Big)\delta A_s^{(n)} \\ &\quad + ig_s\,\tau_{\rm int}\big(\rho_0^*\,\delta A_p^{(n)} + A_{p,0}\,\delta\rho^{*(n)}\big), \\ \delta\rho^{(n+1)} &= \Big(1 - \frac{\Gamma_B}{2}\tau_{\rm rt}\Big)\delta\rho^{(n)} \\ &\quad + ig_\rho\,\tau_{\rm int}\big(A_{s,0}^*\,\delta A_p^{(n)} + A_{p,0}\,\delta A_s^{*(n)}\big). \end{aligned} \tag{19}$$

A phase convention can then be chosen in which the steady-state amplitudes $A_{p,0}$, $A_{s,0}$, and ρ_0 are real up to the fixed Brillouin phase relation:

$$\begin{aligned} \delta A_p^{(n)} &\simeq iA_{p,0}\,\delta\varphi_p^{(n)}, \\ \delta A_s^{(n)} &\simeq iA_{s,0}\,\delta\varphi_s^{(n)}, \\ \delta\rho^{(n)} &\simeq i\rho_0\,\delta\varphi_\rho^{(n)}, \\ \delta S_{\rm in}^{(n)} &\simeq iS_{\rm in,0}\,\delta\varphi_{\rm in}^{(n)}. \end{aligned} \tag{20}$$

This approximation does not assume that amplitude fluctuations are absent in general. Rather, it reflects the quadrature decomposition of the linearized dynamics around a resonant locked steady state. Amplitude-phase coupling terms would arise in the presence of finite optical or acoustic detuning, and such detuning-induced corrections are beyond the scope of the present model.

Under the phase-only approximation, the fluctuation dynamics are reduced to the coupled evolution of the pump, Stokes, and acoustic phases. Physically, the pump phase acts as the external driving variable, while the Stokes and acoustic phases are coupled through the discrete Brillouin interaction and the round-trip acoustic relaxation. Using the steady-state relations together with the threshold condition derived in Sec. IV, the nonlinear coupling terms can be rewritten in terms of steady-state cavity parameters. The resulting phase recursions are

$$\begin{aligned} \delta\varphi_p^{(n+1)} &= \Big(1 - \frac{\gamma}{2}\tau_{\rm int}\Big)\delta\varphi_p^{(n)} - \frac{\gamma}{2}\tau_{\rm int}\frac{|A_{s,0}|^2}{|A_{p,0}|^2_{\rm th}}\big(\delta\varphi_s^{(n)} + \delta\varphi_\rho^{(n)}\big) \\ &\quad + \frac{\gamma}{2}\tau_{\rm int}\Big(1 + \frac{|A_{s,0}|^2}{|A_{p,0}|^2_{\rm th}}\Big)\delta\varphi_{\rm in}^{(n)}, \\ \delta\varphi_s^{(n+1)} &= \Big(1 - \frac{\gamma}{2}\tau_{\rm int}\Big)\delta\varphi_s^{(n)} + \frac{\gamma}{2}\tau_{\rm int}\big(\delta\varphi_p^{(n)} - \delta\varphi_\rho^{(n)}\big), \\ \delta\varphi_\rho^{(n+1)} &= \Big(1 - \frac{\Gamma_B}{2}\tau_{\rm rt}\Big)\delta\varphi_\rho^{(n)} + \frac{\Gamma_B}{2}\tau_{\rm rt}\big(\delta\varphi_p^{(n)} - \delta\varphi_s^{(n)}\big). \end{aligned} \tag{21}$$

Equations (21) provide the discrete-time phase dynamics of the pump, Stokes, and acoustic fields under external pump-phase driving.

To analyze the phase-noise transfer in the frequency domain, we apply the discrete-time Fourier transform to the round-trip-sampled phase fluctuations. For a generic sequence $\varphi^{(n)}$, we define

$$\Phi(\omega) = \sum_{n=-\infty}^{\infty} \varphi^{(n)} e^{-i\omega n\tau_{\rm rt}}, \tag{22}$$

where $\tau_{\rm rt}$ is the cavity round-trip time. Under this transform, a one-step shift in the round-trip index corresponds to multiplication by $e^{i\omega\tau_{\rm rt}}$. Neglecting transient contributions associated with the initial conditions, the phase recursion relations in Eqs. (21) are converted into algebraic equations for the Fourier-domain phase fluctuations $\Phi_p(z)$, $\Phi_s(z)$, $\Phi_\rho(z)$, and $\Phi_{\rm in}(z)$. Using the discrete-time phase recursion relations, the acoustic phase can be eliminated to obtain the transfer function from the input pump phase to the Stokes phase,

$$H_{{\rm in}\to s}(z) = \frac{\Phi_s(z)}{\Phi_{\rm in}(z)} = \frac{\big(\frac{\gamma}{2}\tau_{\rm int}\big)^2\Big(1 + \frac{|A_{s,0}|^2}{|A_{p,0}|^2_{\rm th}}\Big)}{(z-1)^2 + \big(\gamma\tau_{\rm int} + \frac{\Gamma_B}{2}\tau_{\rm rt}\big)(z-1) + \frac{\gamma}{2}\tau_{\rm int}\big(\frac{\gamma}{2}\tau_{\rm int} + \frac{\Gamma_B}{2}\tau_{\rm rt}\big)\Big(1 + \frac{|A_{s,0}|^2}{|A_{p,0}|^2_{\rm th}}\Big)}. \tag{23}$$

The transfer function $H_{{\rm in}\to s}(z)$ characterizes the frequency-dependent transfer of pump-phase fluctuations to the Stokes phase. Here the complex variable z is associated with the discrete-time Fourier transform defined in Eq. (22). Since the index n labels successive cavity round trips separated by the round-trip time $\tau_{\rm rt}$, a harmonic phase fluctuation at Fourier frequency ω corresponds to

$$z = e^{i\omega\tau_{\rm rt}}. \tag{24}$$

In laser noise analysis, the directly measurable quantity is often the frequency fluctuation rather than the optical phase itself. The instantaneous frequency fluctuation associated with a phase fluctuation $\varphi(t)$ is given by [36]

$$\delta\nu(t) = \frac{1}{2\pi}\frac{d\varphi(t)}{dt}. \tag{25}$$

Therefore, the phase-noise and frequency-noise spectra are related by

$$S_\nu(\omega) = \left(\frac{\omega}{2\pi}\right)^2 S_\varphi(\omega), \tag{26}$$

where $S_\varphi(\omega)$ and $S_\nu(\omega)$ denote the phase-noise and frequency-noise power spectral densities, respectively.

Using the phase transfer function and the phase-to-frequency conversion above, the Stokes frequency-noise spectrum is related to the input pump frequency-noise spectrum by

$$S_{\nu_s}(\omega) = |H_{\rm in\to s}(e^{i\omega\tau_{\rm rt}})|^2\, S_{\nu_{\rm in}}(\omega). \tag{27}$$

Here $S_{\nu_{\rm in}}(\omega)$ denotes the input pump frequency-noise spectrum. Equation (27) therefore predicts the Stokes frequency-noise spectrum from the pump noise spectrum and the discrete-cavity transfer function.

To quantify the noise suppression provided by the Brillouin laser, we introduce the ratio between the input pump frequency-noise spectrum and the resulting Stokes frequency-noise spectrum. Physically, this ratio measures how strongly pump frequency noise is suppressed during the Brillouin conversion process inside the cavity. Accordingly, we define the spectral noise-suppression ratio as

$$\mathcal{C}(\omega) \equiv \frac{S_{\nu_{\rm in}}(\omega)}{S_{\nu_s}(\omega)} = \frac{1}{|H_{\rm in\to s}(e^{i\omega\tau_{\rm rt}})|^2}. \tag{28}$$

Here $S_{\nu_{\rm in}}(\omega)$ and $S_{\nu_s}(\omega)$ denote the frequency-noise power spectral densities of the input pump and the generated Stokes field, respectively. Because $\mathcal{C}(\omega)$ is defined as a ratio of frequency-noise power spectral densities, it is the square of the corresponding amplitude-level phase- or frequency-fluctuation suppression factor. In the low-frequency limit $\omega \to 0$, Eq. (28) reduces to

$$\mathcal{C}(0) = \left(1 + \frac{\Gamma_B\,\tau_{\rm rt}}{\gamma\,\tau_{\rm int}}\right)^2. \tag{29}$$

Equation (29) is the discrete-cavity counterpart of the continuous-medium result in Eq. (7). The difference between the two expressions arises from the different timescales over which optical coupling and acoustic relaxation accumulate. In the continuous-medium model, the optical and acoustic fields remain continuously coupled throughout the cavity evolution, so the suppression is governed by the rate ratio Γ_B/γ_s. In the free-space discrete cavity, by contrast, the nonlinear Brillouin interaction is accumulated only during the short interaction time $\tau_{\rm int}$, whereas the acoustic relaxation accumulates over the full round-trip time $\tau_{\rm rt}$. The relevant effective ratio is therefore changed from the continuous-medium ratio Γ_B/γ_s to the discrete-cavity ratio $\Gamma_B/\gamma \times \tau_{\rm rt}/\tau_{\rm int}$. This result shows explicitly that the low-frequency noise suppression in a free-space Brillouin laser is governed not only by the material acoustic damping rate and the optical decay rate, but also by the separation between the full cavity round-trip time and the much shorter nonlinear interaction time inside the gain medium. The passive free-space propagation segment is therefore an essential part of the noise dynamics. During this stage, the optical field continues to circulate in the cavity, while the acoustic field remains localized in the gain medium and continues to decay in the absence of further optical driving. This interaction-propagation separation effectively enhances the acoustic damping at the cavity level and explains why unusually large noise-suppression ratios can arise in free-space Brillouin-laser experiments.

To validate the pump-noise transfer function derived above, we performed time-domain simulations of the discrete-cavity dynamics using the parameters listed in Table I. The input pump was modeled with white frequency noise corresponding to a Lorentzian linewidth of 3 kHz. This imposed noise source was used as a controlled test input, allowing a direct comparison between the simulated Stokes response and the analytical transfer-function prediction. Figure 3(a) shows the simulated phase trajectories. The pump phase exhibits large random excursions characteristic of a diffusive phase process, whereas the Stokes phase remains strongly confined around zero with only small residual fluctuations. This contrast directly reflects the strong phase-noise suppression produced by the discrete-cavity dynamics. A more quantitative validation is provided by the frequency-noise spectra shown in Fig. 3(b). The blue curve denotes the imposed pump frequency-noise spectrum, which remains nearly flat over the analyzed offset-frequency range, consistent with the white frequency-noise input. The red curve shows the simulated Stokes frequency-noise spectrum, while the dashed black curve represents the analytical prediction obtained from Eq. (28). The agreement between the simulated Stokes spectrum and the analytical prediction confirms that the transfer function captures the pump-phase-noise filtering of the discrete cavity. The resulting Stokes frequency-noise level is also of the same order as the experimentally reported value of approximately 3 $\mathrm{Hz}^2/\mathrm{Hz}$ over the offset-frequency range from 10^3 to 10^6 Hz [31]. This comparison should be understood as a consistency check of the predicted noise-suppression scale, rather than a direct fit to measured pump- and Stokes-noise spectra.

B. Fundamental linewidth from thermal noise

So far, we have considered the deterministic cavity response and the transfer of external pump noise in the absence of internal stochastic driving. To determine the fundamental noise limit of the Brillouin laser, it is necessary to include the thermal fluctuations of the acoustic density wave explicitly. Because the acoustic mode is coupled to a finite-temperature reservoir, it is subject not only to deterministic damping but also to random Langevin forcing. Such thermally driven acoustic fluctuations are the physical origin of the phonon-limited linewidth of Brillouin lasers, as demonstrated in cryogenic microresonator experiments [37]. They persist even in the absence of technical pump noise and therefore

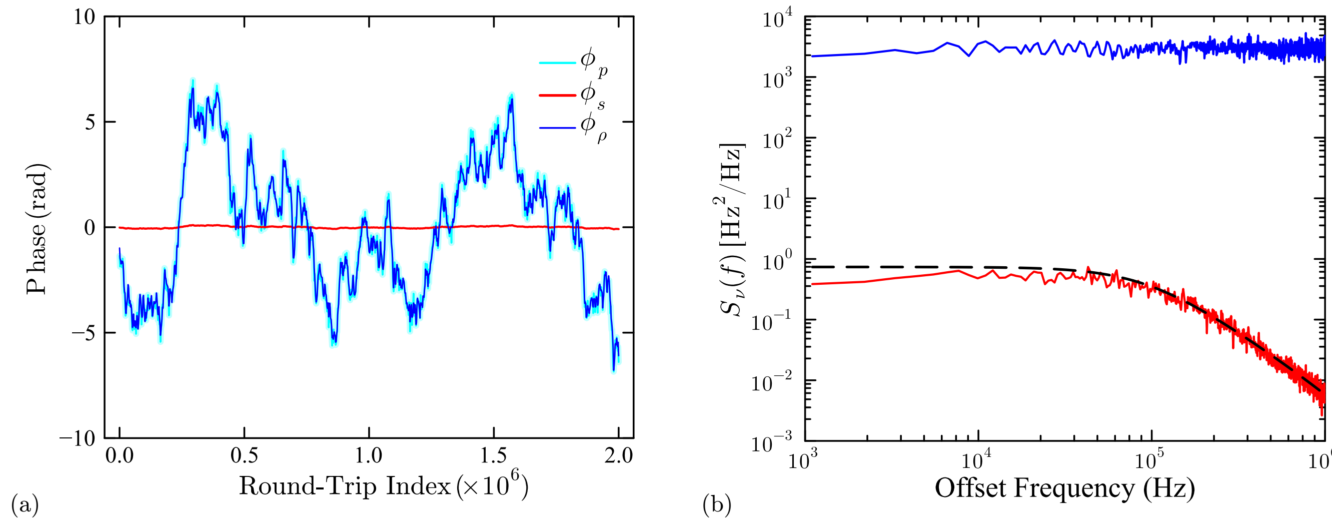

FIG. 3. (a) Simulated phase evolution versus round-trip index under an imposed white pump-frequency-noise input. The blue curve represents the pump phase, while the red curve denotes the Stokes phase. (b) Frequency-noise spectra obtained from the same simulation. The blue curve shows the imposed pump frequency-noise spectrum, the red curve shows the simulated Stokes frequency-noise spectrum, and the dashed black curve gives the analytical prediction from Eq. (28).

set the fundamental floor for the Stokes linewidth and relative intensity noise.

To evaluate the intrinsic linewidth, we now consider the thermally driven phase dynamics of the discrete cavity. Compared with the phase-recursion equations (21) used above for pump-noise transfer, the present formulation removes the external input pump-phase fluctuation as the driving term and instead introduces a stochastic Langevin contribution in the acoustic equation. In this way, the deterministic coupling between the pump, Stokes, and acoustic phases remains unchanged, while the only stochastic drive is provided by the thermally excited acoustic field. Linearizing the stochastic discrete-cavity equations around the steady-state operating point and retaining only phase fluctuations to leading order, we obtain the following recursion relations:

$$\begin{aligned}
\delta\varphi_p^{(n+1)} &= \left(1-\frac{\gamma}{2}\tau_{\mathrm{int}}\right)\delta\varphi_p^{(n)} - \frac{\gamma}{2}\tau_{\mathrm{int}}\frac{|A_{s,0}|^2}{|A_{p,0}|^2_{\mathrm{th}}}\left(\delta\varphi_s^{(n)}+\delta\varphi_\rho^{(n)}\right),\\
\delta\varphi_s^{(n+1)} &= \left(1-\frac{\gamma}{2}\tau_{\mathrm{int}}\right)\delta\varphi_s^{(n)} + \frac{\gamma}{2}\tau_{\mathrm{int}}\left(\delta\varphi_p^{(n)}-\delta\varphi_\rho^{(n)}\right),\\
\delta\varphi_\rho^{(n+1)} &= \left(1-\frac{\Gamma_B}{2}\tau_{\mathrm{rt}}\right)\delta\varphi_\rho^{(n)} + \frac{\Gamma_B}{2}\tau_{\mathrm{rt}}\left(\delta\varphi_p^{(n)}-\delta\varphi_s^{(n)}\right)+\eta^{(n)}.
\end{aligned} \tag{30}$$

Here $\eta^{(n)}$ denotes the stochastic phase increment induced by the thermal Langevin force acting on the acoustic mode. The corresponding discrete acoustic fluctuation over one round trip is obtained by integrating the continuous noise force,

$$F_\rho^{(n)} = \int_{n\tau_{\mathrm{rt}}}^{(n+1)\tau_{\mathrm{rt}}} f_B(t)\,dt, \tag{31}$$

where $f_B(t)$ is the complex white-noise force introduced in Appendix B. The phase noise entering the linearized phase dynamics is obtained by projecting this complex increment onto the acoustic phase quadrature,

$$\eta^{(n)} = \frac{\mathrm{Im}\left[F_\rho^{(n)}\rho_0^*\right]}{|\rho_0|^2}, \tag{32}$$

so that only the component of the fluctuation orthogonal to the steady-state acoustic amplitude contributes to phase diffusion.

Following the same procedure as in the pump-noise transfer analysis, we apply the discrete-time Fourier transform defined in Eq. (22) to the stochastic phase recursion relations in Eq. (30) and neglect the transient contributions associated with the initial conditions. This converts the discrete recursion relations into algebraic equations in the frequency domain. Eliminating the pump and acoustic phase variables then yields the transfer relation from the thermal Langevin increment η to the Stokes phase fluctuation, which can be written as

$$H_{\eta\to s}(z) \equiv \frac{\Phi_s(z)}{\eta(z)} = -\frac{\frac{\gamma}{2}\tau_{\mathrm{int}}\left[(z-1)+\frac{\gamma}{2}\tau_{\mathrm{int}}\left(1+\frac{|A_{s,0}|^2}{|A_{p,0}|^2_{\mathrm{th}}}\right)\right]}{(z-1)\left[(z-1)^2+\left(\gamma\tau_{\mathrm{int}}+\frac{\Gamma_B}{2}\tau_{\mathrm{rt}}\right)(z-1)+\frac{\gamma}{2}\tau_{\mathrm{int}}\left(\frac{\gamma}{2}\tau_{\mathrm{int}}+\frac{\Gamma_B}{2}\tau_{\mathrm{rt}}\right)\left(1+\frac{|A_{s,0}|^2}{|A_{p,0}|^2_{\mathrm{th}}}\right)\right]}. \tag{33}$$

The Stokes frequency-noise spectrum generated by the thermal Langevin force is therefore given by

$$S_{\nu_s}(\omega) = \left(\frac{\omega}{2\pi}\right)^2 |H_{\eta\to s}(e^{i\omega\tau_{\mathrm{rt}}})|^2 S_\eta(\omega), \tag{34}$$

where $S_\eta(\omega)$ denotes the power spectral density of the acoustic Langevin phase increment. The factor $(z-1)^{-1}$ in $H_{\eta\to s}(z)$ reflects the diffusive accumulation of phase fluctuations and therefore corresponds to the usual phase-diffusion pole at low frequency. This apparent singular behavior is removed when passing from phase noise to frequency noise, because the time derivative relating frequency to phase contributes a compensating factor proportional to $(z-1)$ in the low-frequency limit. As a result, the Stokes frequency-noise spectrum remains finite as $\omega \to 0$, and its zero-frequency value determines the fundamental white frequency-noise floor. And the discrete acoustic phase noise corresponds to a white-noise process with spectral density

$$S_\eta(\omega) = \langle \eta^{(n)}\eta^{(n)} \rangle = \frac{\tau_{rt} C_B}{2|\rho_0|^2}, \tag{35}$$

where C_B denotes the discrete acoustic Langevin noise strength, which in the weak-damping limit can be written as

$$C_B \simeq \frac{k_B T \rho_m \Gamma_B}{v^2 V_{\text{opt}}} \tau_{\text{int}}. \tag{36}$$

Here k_B is the Boltzmann constant, T is the temperature, and V_{opt} denotes the effective optical mode volume participating in the Brillouin interaction. This expression follows from the fluctuation-dissipation [38] relation for thermally driven acoustic fluctuations (see Appendix B).

Because the intrinsic linewidth is set by the white low-frequency floor of the frequency-noise spectrum, we evaluate the zero-frequency limit of Eq. (34). In this limit, the phase-diffusion pole contained in the Langevin transfer function is canceled by the phase-to-frequency conversion, leaving a finite white frequency-noise plateau. The zero-frequency Stokes frequency-noise floor is then obtained as

$$S_{\nu,s}(0) = \frac{1}{(2\pi)^2 \tau_{\text{rt}}^2} \frac{(\gamma \tau_{\text{int}})^2}{(\gamma \tau_{\text{int}} + \Gamma_B \tau_{\text{rt}})^2} S_\eta(0). \tag{37}$$

For white frequency noise, the intrinsic linewidth is directly determined by this low-frequency plateau [36]. Using the acoustic Langevin noise spectrum defined above Eq. (35), we obtain

$$\Delta\nu_{\text{int}} = \frac{C_B}{8\pi^2 |\rho_0|^2 \tau_{\text{rt}}} \frac{1}{\left(1 + \frac{\Gamma_B \tau_{\text{rt}}}{\gamma \tau_{\text{int}}}\right)^2}. \tag{38}$$

To verify the analytical prediction for the intrinsic noise floor, we performed numerical simulations including the thermal Langevin force acting on the acoustic mode. The stochastic increment $\eta^{(n)}$ was activated in the acoustic phase equation, representing thermally driven acoustic fluctuations in the absence of external pump noise. From the simulated phase trajectories, the corresponding frequency-noise spectrum of the Stokes field was extracted. As shown in Fig. 4, the red curve represents the simulated spectrum, while the dashed black line denotes the analytical prediction of Eq. (37). The spectrum exhibits a flat low-frequency plateau characteristic of white frequency noise, which directly determines the intrinsic linewidth. The excellent agreement between the simulated noise floor and the theoretical prediction confirms the validity of the analytical model for the fundamental noise limit.

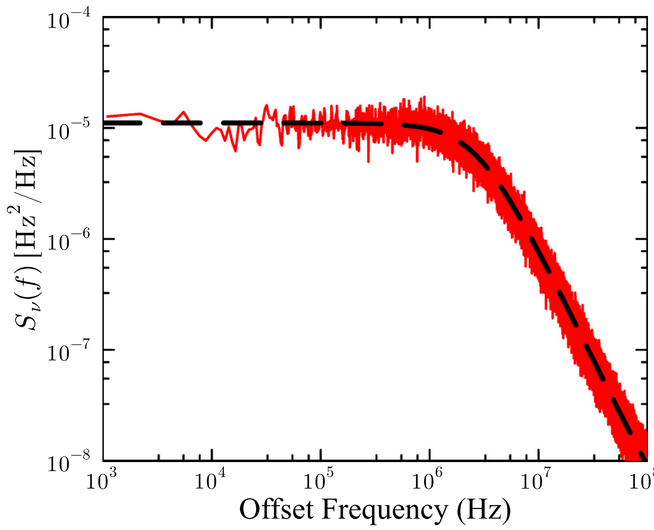

FIG. 4. Simulated fundamental frequency-noise spectrum of the Stokes field (red). The dashed black curve shows the theoretical prediction.

C. Relative intensity noise

We now analyze the relative intensity noise (RIN) of the Stokes field by projecting the linearized dynamics onto the amplitude quadrature. Under the same resonant, phase-locked operating condition used in Sec. V A, the amplitude and phase quadratures are decoupled to first order. The pump-phase fluctuations and the thermal Langevin force are therefore set to zero, so that pump intensity modulation remains the only external driving source. The optical and acoustic fields, together with the input pump field, are therefore written as

$$\begin{aligned} A_p^{(n)} &= A_{p,0}\big(1+\delta u_p^{(n)}\big), \\ A_s^{(n)} &= A_{s,0}\big(1+\delta u_s^{(n)}\big), \\ \rho^{(n)} &= \rho_0\big(1+\delta u_\rho^{(n)}\big), \\ S_{\text{in}}^{(n)} &= S_{\text{in},0}\big(1+\delta u_{S_{\text{in}}}^{(n)}\big), \end{aligned} \tag{39}$$

where $\delta u_p^{(n)}$, $\delta u_s^{(n)}$, $\delta u_\rho^{(n)}$, and $\delta u_{S_{\text{in}}}^{(n)}$ denote small real amplitude perturbations about the steady-state values.

Since the relative intensity noise is defined in terms of normalized intensity fluctuations, the RIN transfer function is naturally defined as the ratio between the normalized Stokes intensity perturbation and the normalized input pump intensity perturbation. For pure amplitude perturbations, one has $\delta I_s/I_{s,0} \simeq 2\delta u_s^{(n)}$ and $\delta I_{\text{in}}/I_{\text{in},0} \simeq 2\delta u_{S_{\text{in}}}^{(n)}$, so that the corresponding RIN transfer function reduces to

$$H_{\text{RIN}}(z) \equiv \frac{\delta u_s(z)}{\delta u_{S_{\text{in}}}(z)}. \tag{40}$$

Substituting the perturbative expansions into the linearized round-trip equations and transforming the system into the z domain yields a set of algebraic relations describing the discrete-cavity response to pump intensity modulation. Solving these equations for $\delta u_s(z)$ in terms of the input fluctuation $\delta u^{(n)}_{S_{\rm in}}(z)$ yields the RIN transfer function,

$$H_{\rm RIN}(z) = \frac{\left(\frac{\gamma}{2}\tau_{\rm int}\right)^2\left(1+\frac{|A_{s,0}|^2}{|A_{p,0}|^2_{\rm th}}\right)\left(\Delta_b+\frac{\Gamma_B}{2}\tau_{\rm rt}\right)}{\Delta_b\Delta_p^2+\left(\frac{\gamma}{2}\tau_{\rm int}\right)\left(\frac{\Gamma_B}{2}\tau_{\rm rt}\right)\frac{|A_{s,0}|^2}{|A_{p,0}|^2_{\rm th}}\,\Delta_p+\left(\frac{\gamma}{2}\tau_{\rm int}\right)^2\frac{|A_{s,0}|^2}{|A_{p,0}|^2_{\rm th}}\,\Delta_b+2\left(\frac{\gamma}{2}\tau_{\rm int}\right)^2\left(\frac{\Gamma_B}{2}\tau_{\rm rt}\right)\frac{|A_{s,0}|^2}{|A_{p,0}|^2_{\rm th}}}, \tag{41}$$

where the shorthand quantities are defined as

$$\Delta_p = z-\left(1-\frac{\gamma}{2}\tau_{\rm int}\right),$$
$$\Delta_b = z-\left(1-\frac{\Gamma_B}{2}\tau_{\rm rt}\right). \tag{42}$$

The RIN spectrum of the Stokes field can then be obtained directly from the transfer function. For a linear system, the output noise spectrum is given by the input spectrum multiplied by the squared magnitude of the transfer function. Accordingly, the Stokes RIN spectrum reads

$$\mathrm{RIN}_s(\omega) = |H_{\rm RIN}(\omega)|^2\,\mathrm{RIN}_{\rm in}(\omega). \tag{43}$$

To characterize the low-frequency behavior of the intensity noise, we consider the zero-frequency limit of the transfer function. Substituting $z\to 1$ into Eq. (41) yields the low-frequency RIN transfer factor:

$$|H_{\rm RIN}(1)|^2 = \left|\frac{2\left(1+\frac{|A_{s,0}|^2}{|A_{p,0}|^2_{\rm th}}\right)}{1+4\frac{|A_{s,0}|^2}{|A_{p,0}|^2_{\rm th}}}\right|^2. \tag{44}$$

This result shows that the low-frequency RIN transfer is determined by the operating point above threshold. Near threshold, the generated Stokes field is weak, so a small pump-intensity modulation produces a large fractional change in the Stokes intensity; consequently, $|H_{\rm RIN}(1)|\to 2$, corresponding to a RIN power-transfer factor of 4. Far above threshold, the intracavity pump is more strongly clamped and additional pump-intensity modulation is converted less efficiently into fractional Stokes-power modulation; in this limit, $|H_{\rm RIN}(1)|\to 1/2$, corresponding to a RIN power-transfer factor of 1/4. Thus, unlike the phase-noise response, the low-frequency RIN is governed by the differential response of the steady-state Stokes output to pump-power fluctuations rather than by acoustic phase filtering.

To validate the analytical RIN transfer model, we performed numerical simulations by introducing controlled amplitude modulation on the input pump field in the discrete-cavity map. This modulation serves as the sole external intensity-noise source and drives the coupled optical-acoustic amplitude dynamics. The Stokes RIN spectrum was then extracted from the normalized Stokes intensity fluctuations. Figure 5 shows the result. The red curve denotes the simulated Stokes RIN spectrum, while the dashed black curve represents the analytical prediction obtained from the linearized transfer function. At low offset frequencies, the Stokes RIN follows the pump RIN with the operating-point-dependent transfer factor predicted by Eq. (44). This behavior reflects the quasistatic conversion of pump-power fluctuations into Stokes-power fluctuations through the steady-state input-output response. At higher offset frequencies, the acoustic mode and intracavity Stokes field cannot follow rapid pump-amplitude fluctuations adiabatically, so the Stokes RIN rolls off. The pole structure of Eq. (44) reproduces this roll-off, and the agreement between the simulated and analytical spectra confirms that the linearized amplitude block captures the intensity-noise transfer dynamics. This behavior is consistent with the RIN response previously reported for microcavity Brillouin lasers [30].

VI. CONCLUSION

In this work, we have developed a discrete-cavity model for free-space Brillouin lasers. In contrast to conventional continuous-medium descriptions, the present model treats the short nonlinear interaction inside the gain medium and the subsequent free-space propagation as two distinct stages of each cavity round trip. This interaction-propagation separation introduces a temporal asymmetry between the optical and acoustic dynamics: the optical fields circulate over the full round trip, whereas the acoustic field remains localized in the gain medium and relaxes during the passive propagation interval. From the viewpoint of the round-trip optical dynamics, this asymmetry appears as an enhanced effective acoustic damping. Based on this discrete-cavity model, we derived analytical results for the pump-noise suppression ratio, the fundamental intrinsic linewidth, and the relative intensity noise of free-space Brillouin lasers. The theoretical predictions are consistent with the reported output-power and noise-suppression scales, indicating that the present model captures the essential physical mechanism

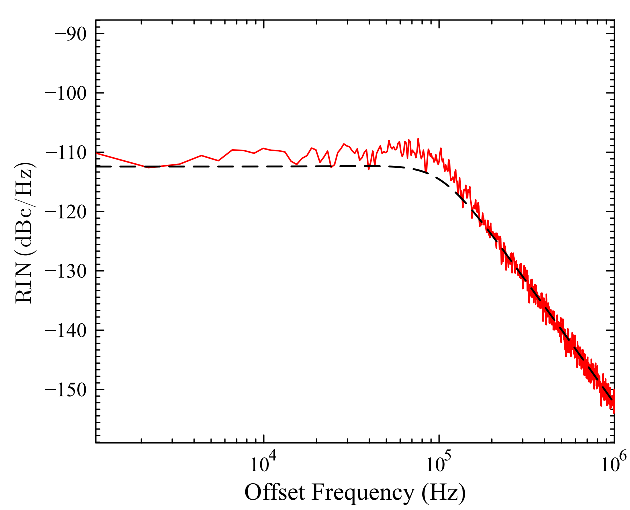

FIG. 5. Relative intensity noise spectrum of the Stokes field under controlled pump-intensity modulation. The solid red line denotes the simulated Stokes RIN, while the dashed black line indicates the theoretical prediction.

that is absent in conventional continuous-medium theories. These results provide a cavity-level theoretical description of free-space Brillouin lasers and complement established continuous-medium Brillouin-laser theory. Free-space Brillouin lasers are distinguished by their power scalability to the watt level. The present results show that such systems can simultaneously exhibit strong noise suppression and ultralow fundamental noise. This combination of high power and low noise makes free-space Brillouin lasers promising for applications requiring both spectral purity and power scalability.

ACKNOWLEDGMENTS

J.P. acknowledges support from the Research School of Advanced Photon Science of the Helmholtz Institute Jena. Z.B. acknowledges support from the National Key Research and Development Program of China (Grant No. 2024YFE0206000) and the National Natural Science Foundation of China (Grant No. 62375076).

DATA AVAILABILITY

There are no publicly available research data or software supporting this article. Requests for further information or data should be sent to the authors.

APPENDIX A: DERIVATION OF THE DELTA-KICK INTERACTION UPDATE

Within the nonlinear gain medium, the slowly varying envelopes of the pump field $A_p(t)$, the Stokes field $A_s(t)$, and the acoustic density wave $\rho(t)$ obey the driven three-wave coupling equations given in Eqs. (5). Since the interaction takes place only over the short time interval $\tau_{\rm int}$, we approximate the evolution during a single pass through the gain medium to first order in $\tau_{\rm int}$. The nonlinear coupling terms are evaluated using the preinteraction amplitudes $A_p^{(n)}$, $A_s^{(n)}$, and $\rho^{(n)}$, which are assumed to remain approximately constant during one pass. This yields

$$\begin{aligned} A_p^{(n,+)} &\approx \left(1-\frac{\gamma}{2}\tau_{\rm int}\right)A_p^{(n)} + \frac{i\omega_p\gamma_e}{4n^2\rho_m}\Lambda_p\,\tau_{\rm int}\,\rho^{(n)}A_s^{(n)} \\ &\quad + \sqrt{\kappa_{\rm ex}}\,\tau_{\rm int}S_{\rm in}, \\ A_s^{(n,+)} &\approx \left(1-\frac{\gamma}{2}\tau_{\rm int}\right)A_s^{(n)} + \frac{i\omega_s\gamma_e}{4n^2\rho_m}\Lambda_s\,\tau_{\rm int}\,\rho^{*(n)}A_p^{(n)}, \\ \rho^{(n,+)} &\approx \left(1-\frac{\Gamma_B}{2}\tau_{\rm int}\right)\rho^{(n)} + i\frac{\epsilon_0\gamma_e^2q^2}{4\Omega}\Lambda_\rho\,\tau_{\rm int}\,A_p^{(n)}A_s^{*(n)}. \end{aligned} \tag{A1}$$

We then introduce the effective coupling coefficients

$$g_p \equiv \frac{\omega_p\gamma_e}{4n^2\rho_m}\Lambda_p,\quad g_s \equiv \frac{\omega_s\gamma_e}{4n^2\rho_m}\Lambda_s,\quad g_\rho \equiv \frac{\epsilon_0\gamma_e^2q^2}{4\Omega}\Lambda_\rho, \tag{A2}$$

so that the interaction step can be written in the compact form

$$\begin{aligned} A_p^{(n,+)} &= \left(1-\frac{\gamma}{2}\tau_{\rm int}\right)A_p^{(n)} + ig_p\,\tau_{\rm int}\,\rho^{(n)}A_s^{(n)} + \sqrt{\kappa_{\rm ex}}\,\tau_{\rm int}\,S_{\rm in}, \\ A_s^{(n,+)} &= \left(1-\frac{\gamma}{2}\tau_{\rm int}\right)A_s^{(n)} + ig_s\,\tau_{\rm int}\,\rho^{*(n)}A_p^{(n)}, \\ \rho^{(n,+)} &= \left(1-\frac{\Gamma_B}{2}\tau_{\rm int}\right)\rho^{(n)} + ig_\rho\,\tau_{\rm int}\,A_p^{(n)}A_s^{*(n)}. \end{aligned} \tag{A3}$$

In the reduced round-trip description, the interaction segment is treated as a delta kick, whereas the acoustic decay is taken to accumulate over the full cavity round-trip time $\tau_{\rm rt}$. Accordingly, the acoustic update after one round trip is written as

$$\rho^{(n+1)} = \left(1-\frac{\Gamma_B}{2}\tau_{\rm rt}\right)\rho^{(n)} + ig_\rho\,\tau_{\rm int}\,A_p^{(n)}A_s^{*(n)}. \tag{A4}$$

The optical fields $A_p^{(n,+)}$ and $A_s^{(n,+)}$ represent the amplitudes immediately after the localized interaction. In the reduced round-trip map, the remaining passive propagation is not written as a separate loss channel; instead, the optical loss is absorbed into the lumped optical survival factor used in the sampled map. Thus,

$$A_p^{(n+1)} = A_p^{(n,+)},\quad A_s^{(n+1)} = A_s^{(n,+)}. \tag{A5}$$

Collecting the optical and acoustic updates, we obtain the reduced round-trip map

$$\begin{aligned} A_p^{(n+1)} &= \left(1-\frac{\gamma}{2}\tau_{\rm int}\right)A_p^{(n)} + ig_p\,\tau_{\rm int}\,\rho^{(n)}A_s^{(n)} + \sqrt{\kappa_{\rm ex}}\,\tau_{\rm int}\,S_{\rm in}, \\ A_s^{(n+1)} &= \left(1-\frac{\gamma}{2}\tau_{\rm int}\right)A_s^{(n)} + ig_s\,\tau_{\rm int}\,\rho^{*(n)}A_p^{(n)}, \\ \rho^{(n+1)} &= \left(1-\frac{\Gamma_B}{2}\tau_{\rm rt}\right)\rho^{(n)} + ig_\rho\,\tau_{\rm int}\,A_p^{(n)}A_s^{*(n)}. \end{aligned} \tag{A6}$$

APPENDIX B: THERMAL NOISE IN THE DISCRETE-CAVITY MAP

We start from the deterministic discrete round-trip map introduced in Appendix A. In reality, the acoustic mode is subject to thermal fluctuations. Because the acoustic field experiences damping at rate Γ_B, the fluctuation-dissipation theorem requires the presence of a Langevin force driving the acoustic degree of freedom. We therefore modify the acoustic update equation by adding a stochastic contribution,

$$\rho^{(n+1)} = \left(1-\frac{\Gamma_B}{2}\tau_{\rm rt}\right)\rho^{(n)} + ig_\rho\,\tau_{\rm int}\,A_p^{(n)}A_s^{*(n)} + F_\rho^{(n)}, \tag{B1}$$

where $F_\rho^{(n)}$ denotes the discretized Langevin increment associated with the nth cavity round trip. The discrete noise increment is obtained by integrating the continuous Langevin force over one round-trip interval,

$$F_\rho^{(n)} = \int_{n\tau_{\rm rt}}^{(n+1)\tau_{\rm rt}} f_B(t)\,dt, \tag{B2}$$

where $f_B(t)$ is a complex white-noise force satisfying

$$\langle f_B(t)f_B^*(t')\rangle = C_B^{(c)}\,\delta(t-t'). \tag{B3}$$

According to the fluctuation-dissipation relation, the noise strength of the continuous Langevin force is

$$C_B^{(c)} = \frac{k_BT\rho_m\Gamma_B}{v^2V_{\rm opt}}, \tag{B4}$$

where k_B is the Boltzmann constant, T denotes the temperature, ρ_m is the equilibrium mass density of the medium, Γ_B is the acoustic damping rate, v is the acoustic velocity, and $V_{\rm opt}$

represents the effective optical mode volume participating in the Brillouin interaction.

Although the acoustic mode is coupled to a thermal reservoir throughout the full round trip, the optical fields sample the acoustic fluctuation only during the finite Brillouin interaction interval inside the gain medium. In the delta-kick model, the optoacoustic coupling is therefore represented by a localized temporal window of duration $\tau_{\rm int}$. The Langevin term that enters the optical phase-noise dynamics should consequently be interpreted as the thermally driven acoustic fluctuation projected onto this interaction window, rather than as the total acoustic noise accumulated over the full round trip. With this interpretation, the effective stochastic increment is written as

$$F_\rho^{(n)} = \int_0^{\tau_{\rm int}} e^{-(\Gamma_B/2)(\tau_{\rm int}-t)} f_B^{(n)}(t)\,dt, \tag{B5}$$

where $f_B^{(n)}(t)$ is the continuous Langevin force during the nth interaction event. The exponential factor accounts for acoustic damping within the interaction interval. Using the white-noise correlation

$$\langle f_B(t) f_B^*(t')\rangle = C_B^{(c)}\delta(t-t'), \tag{B6}$$

we obtain

$$\langle F_\rho^{(n)} F_\rho^{(m)*}\rangle = C_B\delta_{nm}, \tag{B7}$$

where

$$C_B = \frac{C_B^{(c)}}{\Gamma_B}(1-e^{-\Gamma_B\tau_{\rm int}}) \simeq C_B^{(c)}\tau_{\rm int}. \tag{B8}$$

The final approximation holds for $\Gamma_B\tau_{\rm int} \ll 1$. This effective-noise description is consistent with the delta-kick approximation used for the deterministic Brillouin coupling: only fluctuations sampled during the localized interaction are converted into optical phase noise. Thermal fluctuations generated during the passive propagation interval are part of the acoustic reservoir, but they are not directly coupled to the optical fields until a subsequent interaction event. A more complete stochastic map could include such round-trip accumulated acoustic noise explicitly; this would modify the effective thermal-noise strength but not the deterministic interaction-propagation mechanism responsible for the pump-noise suppression.

[1] W. Loh, J. Stuart, D. Reens, C. D. Bruzewicz, D. Braje, J. Chiaverini, P. W. Juodawlkis, J. M. Sage, and R. McConnell, Operation of an optical atomic clock with a Brillouin laser subsystem, Nature (London) **588**, 244 (2020).

[2] B. J. Bloom, T. L. Nicholson, J. R. Williams, S. L. Campbell, M. Bishof, X. Zhang, W. Zhang, S. L. Bromley, and J. Ye, An optical lattice clock with accuracy and stability at the 10^{-18} level, Nature (London) **506**, 71 (2014).

[3] H. Häffner, C. F. Roos, and R. Blatt, Quantum computing with trapped ions, Phys. Rep. **469**, 155 (2008).

[4] X. Su, C. Tian, X. Deng, Q. Li, C. Xie, and K. Peng, Quantum entanglement swapping between two multipartite entangled states, Phys. Rev. Lett. **117**, 240503 (2016).

[5] J. Aasi *et al.* (The LIGO Scientific Collaboration), Advanced LIGO, Class. Quantum Gravity **32**, 074001 (2015).

[6] B. P. Abbott *et al.* (LIGO Scientific Collaboration and Virgo Collaboration), Observation of gravitational waves from a binary black hole merger, Phys. Rev. Lett. **116**, 061102 (2016).

[7] R. J. Rafac, B. C. Young, J. A. Beall, W. M. Itano, D. J. Wineland, and J. C. Bergquist, Sub-dekahertz ultraviolet spectroscopy of $^{199}Hg^+$, Phys. Rev. Lett. **85**, 2462 (2000).

[8] D. G. Matei, T. Legero, S. Häfner, C. Grebing, R. Weyrich, W. Zhang, L. Sonderhouse, J. M. Robinson, J. Ye, F. Riehle, and U. Sterr, 1.5 μm lasers with sub-10 mHz linewidth, Phys. Rev. Lett. **118**, 263202 (2017).

[9] W. Jin, Q.-F. Yang, L. Chang, B. Shen, H. Wang, M. A. Leal, L. Wu, M. Gao, A. Feshali, M. Paniccia, K. J. Vahala, and J. E. Bowers, Hertz-linewidth semiconductor lasers using CMOS-ready ultra-high-Q microresonators, Nat. Photon. **15**, 346 (2021).

[10] T. J. Kane and R. L. Byer, Monolithic, unidirectional single-mode Nd:YAG ring laser, Opt. Lett. **10**, 65 (1985).

[11] R. Pant, C. G. Poulton, D.-Y. Choi, H. Mcfarlane, S. Hile, E. Li, L. Thevenaz, B. Luther-Davies, S. J. Madden, and B. J. Eggleton, On-chip stimulated Brillouin scattering, Opt. Express **19**, 8285 (2011).

[12] B. J. Eggleton, C. G. Poulton, P. T. Rakich, M. J. Steel, and G. Bahl, Brillouin integrated photonics, Nat. Photon. **13**, 664 (2019).

[13] M. Tomes and T. Carmon, Photonic micro-electromechanical systems vibrating at X-band (11-GHz) rates, Phys. Rev. Lett. **102**, 113601 (2009).

[14] H. Lee, T. Chen, J. Li, K. Y. Yang, S. Jeon, O. Painter, and K. J. Vahala, Chemically etched ultrahigh-Q wedge-resonator on a silicon chip, Nat. Photon. **6**, 369 (2012).

[15] I. V. Kabakova, R. Pant, D.-Y. Choi, S. Debbarma, B. Luther-Davies, S. J. Madden, and B. J. Eggleton, Narrow linewidth Brillouin laser based on chalcogenide photonic chip, Opt. Lett. **38**, 3208 (2013).

[16] S. Gundavarapu, G. M. Brodnik, M. Puckett, T. Huffman, D. Bose, R. Behunin, J. Wu, T. Qiu, C. Pinho, N. Chauhan, J. Nohava, P. T. Rakich, K. D. Nelson, M. Salit, and D. J. Blumenthal, Sub-hertz fundamental linewidth photonic integrated Brillouin laser, Nat. Photon. **13**, 60 (2019).

[17] N. Chauhan, A. Isichenko, K. Liu, J. Wang, Q. Zhao, R. O. Behunin, P. T. Rakich, A. M. Jayich, C. Fertig, C. W. Hoyt, and D. J. Blumenthal, Visible light photonic integrated Brillouin laser, Nat. Commun. **12**, 4685 (2021).

[18] Y. Mao, C. Zhang, L. Huang, L. Gao, Y. Li, L. Shi, G. Yin, C. Gong, and T. Zhu, Narrow-linewidth microcavity Brillouin laser based on pump-locked high-Q silica microsphere resonator, Appl. Phys. Lett. **126**, 031105 (2025).

[19] J. Li, H. Lee, and K. J. Vahala, Microwave synthesizer using an on-chip Brillouin oscillator, Nat. Commun. **4**, 2097 (2013).

[20] K. O. Hill, B. S. Kawasaki, and D. C. Johnson, cw Brillouin laser, Appl. Phys. Lett. **28**, 608 (1976).

[21] L. F. Stokes, M. Chodorow, and H. J. Shaw, All-fiber stimulated Brillouin ring laser with submilliwatt pump threshold, Opt. Lett. **7**, 509 (1982).

[22] S. P. Smith, F. Zarinetchi, and S. Ezekiel, Narrow-linewidth stimulated Brillouin fiber laser and applications, Opt. Lett. **16**, 393 (1991).

[23] G. Perin, E. Casta, K. Anilkumar, P. Besnard, and S. Trebaol, Hz-level intrinsic linewidth Brillouin fiber laser in the visible range, Opt. Express **33**, 39751 (2025).

[24] K. Hu, I. V. Kabakova, T. F. S. Büttner, S. Lefrancois, D. D. Hudson, S. He, and B. J. Eggleton, Low-threshold Brillouin laser at 2 μm based on suspended-core chalcogenide fiber, Opt. Lett. **39**, 4651 (2014).

[25] Y. Tao, M. Jiang, L. Liu, C. Li, P. Zhou, and Z. Jiang, Single-polarization single-frequency Brillouin fiber laser that emits almost 5 W of power at 1 μm, Opt. Lett. **47**, 1742 (2022).

[26] J. Li, H. Lee, T. Chen, and K. J. Vahala, Characterization of a high coherence, Brillouin microcavity laser on silicon, Opt. Express **20**, 20170 (2012).

[27] W. Loh, S. Yegnanarayanan, F. O'Donnell, and P. W. Juodawlkis, Ultra-narrow linewidth Brillouin laser with nanokelvin temperature self-referencing, Optica **6**, 152 (2019).

[28] K. Ko, D. Suk, D. Kim, S. Park, B. Sen, D.-G. Kim, Y. Wang, S. Dai, X. Wang, R. Wang, B. J. Chun, K.-H. Ko, P. T. Rakich, D.-Y. Choi, and H. Lee, A mid-infrared Brillouin laser using ultra-high-*Q* on-chip resonators, Nat. Commun. **16**, 2707 (2025).

[29] A. Debut, S. Randoux, and J. Zemmouri, Linewidth narrowing in Brillouin lasers: Theoretical analysis, Phys. Rev. A **62**, 023803 (2000).

[30] W. Loh, S. B. Papp, and S. A. Diddams, Noise and dynamics of stimulated-Brillouin-scattering microresonator lasers, Phys. Rev. A **91**, 053843 (2015).

[31] L. Zhang, H. Chen, W. Fan, Y. Wang, Z. Lu, and Z. Bai, Frequency-stabilized ultra-low-noise free-space Brillouin laser in diamond, in *Optica Laser Congress 2025*, Technical Digest Series (Optica Publishing Group, 2025), p. ATu5A.5.

[32] Z. Bai, R. J. Williams, O. Kitzler, S. Sarang, D. J. Spence, Y. Wang, Z. Lu, and R. P. Mildren, Diamond Brillouin laser in the visible, APL Photonics **5**, 031301 (2020).

[33] D. Jin, Z. Bai, Z. Zhao, Y. Chen, W. Fan, Y. Wang, R. P. Mildren, and Z. Lü, Linewidth narrowing in free-space-running diamond Brillouin lasers, High Power Laser Sci. Eng. **11**, e47 (2023).

[34] H. A. Haus, *Waves and Fields in Optoelectronics* (Prentice-Hall, Englewood Cliffs, NJ, 1983).

[35] K. Ikeda, Multiple-valued stationary state and its instability of the transmitted light by a ring cavity system, Opt. Commun. **30**, 257 (1979).

[36] G. D. Domenico, S. Schilt, and P. Thomann, Simple approach to the relation between laser frequency noise and laser line shape, Appl. Opt. **49**, 4801 (2010).

[37] M.-G. Suh, Q.-F. Yang, and K. J. Vahala, Phonon-limited-linewidth of Brillouin lasers at cryogenic temperatures, Phys. Rev. Lett. **119**, 143901 (2017).

[38] R. W. Boyd, K. Rzążewski, and P. Narum, Noise initiation of stimulated Brillouin scattering, Phys. Rev. A **42**, 5514 (1990).